Journal of
Instrumentation

PAPER • **OPEN ACCESS**

A scalable implementation of a 3D magnetic Hall sensor card for mapping and monitoring applications

To cite this article: Lukas Messner *et al* 2025 *JINST* **20** P09003

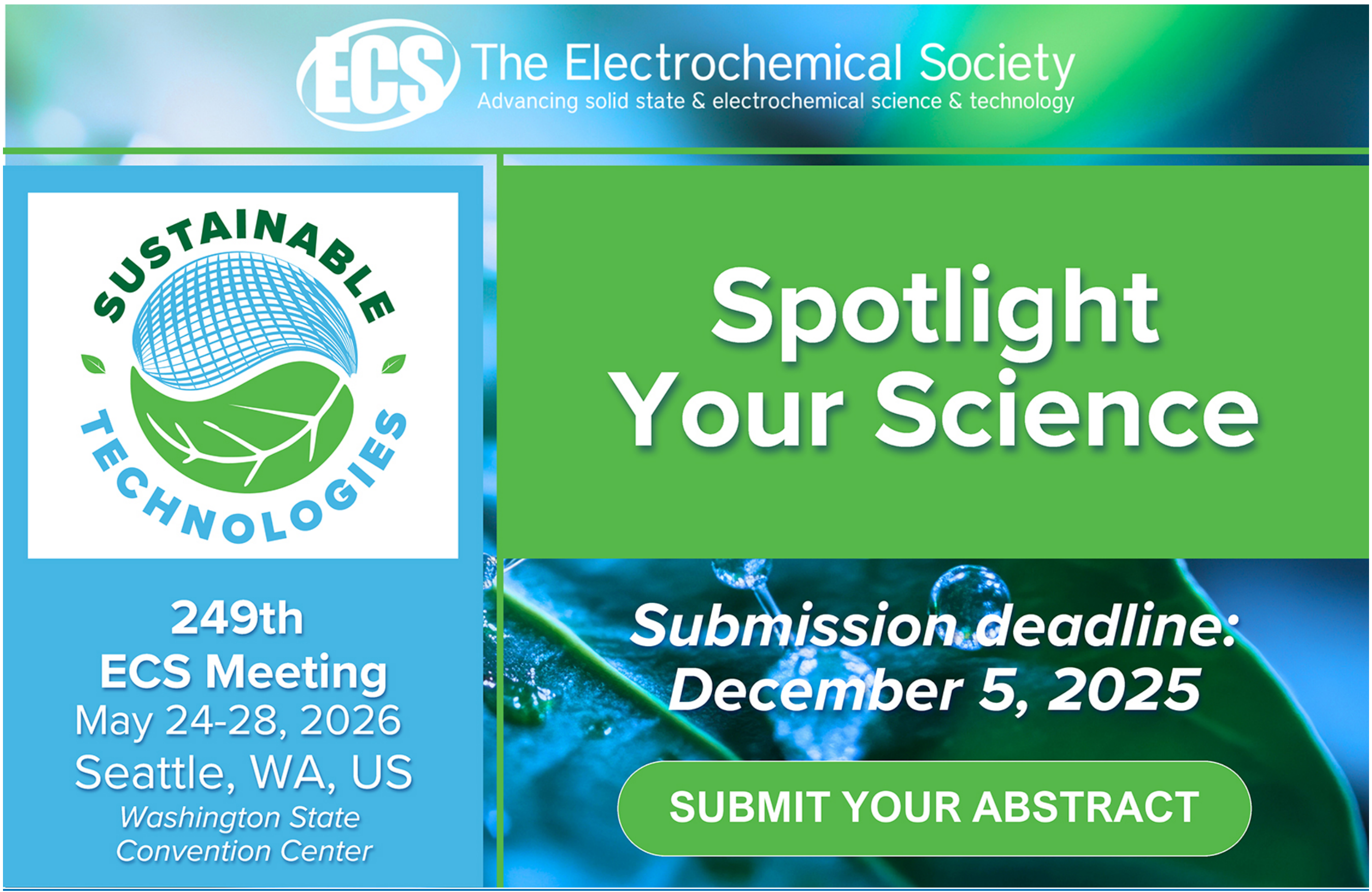

JINST

Published by IOP Publishing for Sissa Medialab

Received: *May 20, 2025*
Revised: *July 15, 2025*
Accepted: *August 18, 2025*
Published: *September 3, 2025*

A scalable implementation of a 3D magnetic Hall sensor card for mapping and monitoring applications

---

Lukas Messner,[a,b,*] **Nicola Pacifico**,[a] **Daniel Baumgarten**[b] **and Raphael Dumps**[a]

[a] *CERN, EP-DT,*
Esplanade des Particules 1, Meyrin, Switzerland
[b] *Biomedical Engineering Group, Department of Mechatronics, University of Innsbruck,*
Technikerstraße 13, Innsbruck, Austria

E-mail: lukas.messner@cern.ch

Abstract: High-energy physics experiments make use of large magnets to bend particle trajectories and thus allow their identification. These magnets, very often custom-built, necessitate an accurate mapping of the generated magnetic field and, in some cases, online monitoring. In both cases, a large number of 3D magnetic field sensors is required, in the order of tens and sometimes hundreds. This article presents the development of an implementation of a 3D Hall sensor card, featuring a custom printed circuit board with a 24-bit $\Delta\Sigma$ analog-to-digital converter, a microcontroller supporting CANopen communication, readout electronics, and an innovative and cost-effective 3-dimensional assembly of the Hall sensor elements, compatible with medium-scale production of up to 200 cards. Initial measurements demonstrate the benefits of the new assembly method and confirm the reliability of the electronic readout in strong magnetic fields up to 1 T. The calibration of the Hall sensor card shows a magnetic field strength measurement precision of 8.8×10^{-5} T, and angular measurement precisions of 0.083° (polar angle) and 0.666° (azimuthal angle). These results were validated at field strengths of 0.225 T, 0.45 T, and 0.675 T. The findings highlight the potential for ongoing optimization and validation in stronger fields up to 4 T.

Keywords: Analogue electronic circuits; Data acquisition concepts; Digital signal processing (DSP)

2025 JINST 20 P09003

---

[*] Corresponding author.

https://doi.org/10.1088/1748-0221/20/09/P09003

Contents

1 **Introduction and requirements** **1**

2 **Hardware architecture** **2**

3 **Cartesian assembly of the Hall sensor elements** **4**

4 **Firmware architecture** **6**

5 **Calibration of the Hall sensor card** **7**
  5.1 Modeling of the calibration setup 7
  5.2 Calibration procedure 8

6 **Experimental results** **9**
  6.1 Electronic readout behaviour 9
  6.2 Hall element alignment precision 10
  6.3 Magnetic field measurements 11

7 **Conclusion** **13**

1 Introduction and requirements

High-energy physics experiments detect particles produced in either particle-particle or particle-fixed-target collisions. Large solenoidal, toroidal, or dipole magnets installed in the experiments bend the trajectories of charged particles, allowing their identification by calculating their momenta using the measured magnetic field strength and the sagitta of their trajectories within the magnetic field. These magnets cover volumes of up to $8000\,\mathrm{m}^3$ (e.g., in the ATLAS experiment) and generate fields as strong as $4\,\mathrm{T}$ (e.g., in the CMS experiment) [1].

Particle identification thus requires the precise knowledge of the magnetic fields within the detector volumes, which is determined through a combination of mapping measurements and simulations. For the mapping of magnetic fields, one typically employs large automatic gantries equipped with accurate 3D magnetic field sensors, which are made to sweep the volume of the magnet.

An example of such an endeavor, detailed in [2], is the mapping campaign carried out in 2006 for the ATLAS solenoid. Subsequently, similar systems were used to map the CMS solenoid in 2008 [3], and the dipole magnet for the NA62 experiment at CERN in 2016 [4]. The mapping systems used in these examples employed 3D Hall sensors, manufactured by incorporating three commercial Hall probes into a Cartesian system. The positioning accuracy of the probes was guaranteed through a complex assembly procedure that incorporated the Hall probes on the three sides of a micro-machined glass cube. While the sensor card presented a good accuracy, its assembly was inherently fragile and its manufacturing labor-intensive due to the manual positioning and connection of the Hall probes on the glass cube.

2025 JINST 20 P09003

This research introduces the development and validation of an accurate 3D Hall sensor card. One requirement of the card is the integration of modern, up-to-date components, ensuring a compact layout, the implementation of a CANopen [5] communication layer directly at the card level, and especially stable and reliable performance in strong magnetic fields. CANopen enables real-time communication with up to 127 sensors, offering compatibility with magnetic environments and long-distance operation over several hundred meters, as well as integration within industrial networks. A key improvement sought in this design is the precise and straightforward Hall element placement, while ensuring a cost-effective assembly process.

Above all, the card is designed to achieve high measurement accuracy in strong magnetic fields, up to 1 T. Currently, the maximum field strength is limited by the available calibration magnet. However, future work will extend the characterization to stronger fields up to 4 T. Previous generations of Hall sensor cards using Hall elements from the same manufacturer have demonstrated reliable performance in fields of 4 T [3], indicating the scalability of the card to higher field strengths. To reach the required accuracy levels, the card must provide a field magnitude resolution in the order of 10^{-4} T [6], angular accuracy in the order of approximately 0.06° [7], and Hall element placement precision within ±0.1 mm [7], in line with the demands of high-energy physics applications. Commercially available solutions do not meet all of these requirements and are unsuitable for the experimental environment.

This paper is structured as follows: in section 2, the hardware and readout electronics are described. Section 3 details the innovative placement of the Hall sensor elements. Section 4 explains the firmware of the card and its integration within a CANopen network. Section 5 outlines the calibration process, which is critical for achieving precise field measurements. Section 6 presents the results, including electronics independence in magnetic fields, alignment precision of the Hall elements, and measurement accuracy. Finally, the conclusions are summarized in section 7.

2 Hardware architecture

The card aims to achieve high accuracy in magnetic field measurements with high stability in temperature and time. Furthermore, the PCB (Printed Circuit Board) size is crucial and should be as small as possible. These requirements are reflected in the selected components and the circuit architecture, all of which were chosen based on their size, accuracy, and stability. The described circuits and components can be seen in figure 1, depicting a block diagram of the schematic (left) and the developed PCB (right).

The two LDOs (Low-dropout Regulators) from Microchip [8] provide a current up to 500 mA for voltages of 3.3 V and 5 V, and they use the small VDFN (Very-thin Dual-flat No-leads) package. Additionally, they meet the requirements by having an output accuracy of 2% and a temperature coefficient of 40 ppm/°C.

As the controlling unit, the STM32L443 microcontroller from STMicroelectronics is used. This application requires one SPI peripheral for communication with the ADC (Analog-to-digital Converter), one CAN peripheral for CAN connectivity, and three pins for feedback LEDs. The crystal resonator used with the microcontroller has a nominal frequency of 10 MHz, with a tolerance of ±20 ppm and a stability of ±30 ppm. The crystal ages at a maximum rate of ±5 ppm per year [9]. The microcontroller has 256 kbytes of flash memory, ensuring sufficient storage for the calibration parameters described in section 5. Furthermore, the 80 MHz processor allows the calculation of calibrated field values

2025 JINST 20 P09003

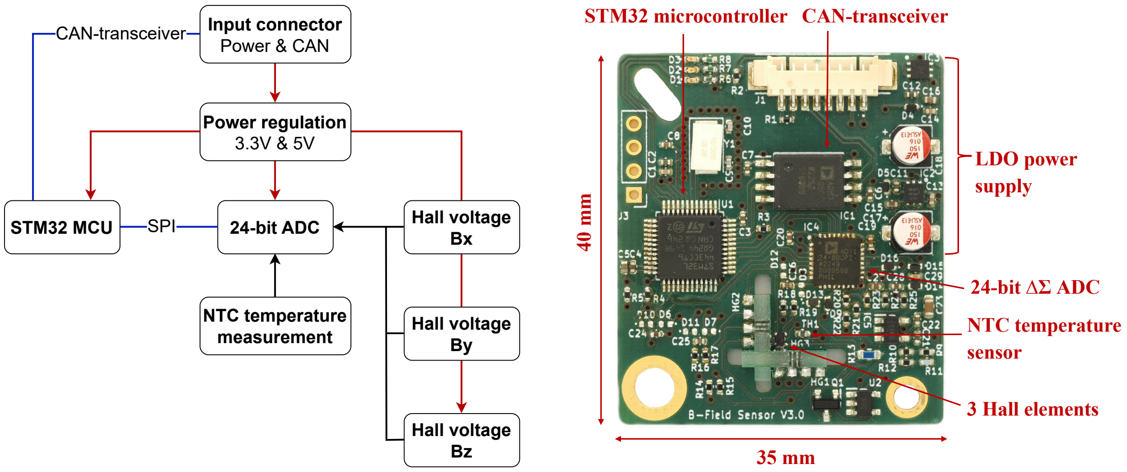

Figure 1. Block diagram of the 3D Hall sensor (left) and the corresponding PCB, featuring a 24-bit ΔΣ ADC for precise temperature and Hall voltage measurements, and a STM32 microcontroller enabling CANopen communication (right).

and their direct publication on the CAN bus. This feature is not yet implemented in the current development stage but will be addressed in future work.

The digitization of the Hall voltages is performed by a 24-bit ΔΣ ADC with a single modulator and multiplexed input channels. The chosen AD7124-8 from Analog Devices [10] has 16 input pins that are combined into eight differential input channels. It includes a programmable gain amplifier that can be used for each channel, and supports self and system calibration routines. The ADC uses an internal frequency clock and provides an internal reference voltage of 2.5 V. Additionally, it offers the option to use two external reference voltages and to generate different currents on three output pins. These features are useful for measuring temperature and Hall voltages.

The application requires high-precision temperature measurement close to the Hall elements. The card is designed to operate within a temperature range of 0 °C to 100 °C. In this range, Murata's NTC (Negative Temperature Coefficient) sensors, known for their fast response time, high sensitivity, and low cost, offer a low tolerance of ±0.1 °C to ±0.2 °C. The selected NTC has a resistance ranging from 27 444.2 Ω to 976 Ω within the desired temperature range [11]. To maximize ADC performance, the full reference range is utilized by setting the ADC reference voltage to match the sensor's maximum resistance value, 27 444.2 Ω. The ADC supports system gain and offset calibration, allowing exclusion of the sensor's minimum resistance value (976 Ω) from the ADC range through offset calibration. Consequently, two additional reference voltages are required alongside the sensor measurement voltage. This is realized by using the ADC's constant current source in a ratiometric design, which negates the effect of current supply variations because the measured voltage is proportional to the reference voltage [12]. The ADC provides a constant current of $I_{\mathrm{Ref}} = 50\,\mu\mathrm{A}$ through series connected reference resistors $R_1 = 27\,444.2\,\Omega$, $R_2 = 976\,\Omega$, and the NTC sensor. This current generates $V_{\mathrm{Ref}} = 1.37\,\mathrm{V}$ across R_1, which serves as the ADC's reference voltage, representing the maximum voltage drop across the NTC. The voltage $V_{\mathrm{Min}} = 0.05\,\mathrm{V}$ across R_2 is used for offset calibration as it corresponds to the NTC's minimum voltage drop. Using resistors with 0.1% accuracy ensures high precision in temperature measurements.

This design utilizes three GaAs HG-0813 Hall elements from Asahi Kasei Microdevices [13], each with an input resistance of $R_{\mathrm{In}} = 1250\,\Omega$ and a sensitivity of $0.24\,\mathrm{V\,T^{-1}}$, assuming a linear dependency and an excitation current of 0.6 mA. The readout is designed for a maximum magnetic field of 1.25 T, offering a margin above the current calibration limit of 1 T and resulting in well-scaled parameter values. For a magnetic field of 1.25 T, the maximum differential output voltage of each Hall elements is ±0.3 V. To ensure precise and stable excitation currents, the elements are connected in series and regulated by a precision current sink with a voltage reference. This current sink is based on the highly accurate REF4132 2.5 V reference with a precision of 0.05%, temperature stability of 12 ppm/°C, and long-term stability of 30 ppm/1000h [14]. A voltage divider with high-precision resistors, along with an operational amplifier and a N-channel MOSFET, provides the necessary 0.3 V for the current source. This voltage, combined with a precision resistor, defines the excitation current as $I_{\mathrm{Exc}} = \frac{0.3\,\mathrm{V}}{500\,\Omega} = 0.6\,\mathrm{mA}$ [15]. This voltage is also routed to an ADC input, where it serves as a gain calibration voltage corresponding to the maximum output voltage of the Hall elements and allows monitoring of the excitation current. The Hall element's output voltage is amplified by the ADC with a factor of 2. To utilize the full ADC reference range and optimize performance, a precision voltage divider derives a 0.6 V reference for the ADC reference voltage. For higher magnetic fields, the reference values for the current source can be adjusted as needed.

3 Cartesian assembly of the Hall sensor elements

The three Hall elements are positioned in a 3-dimensional Cartesian configuration, in order to capture the three components of the magnetic flux vector $\vec{B}$, with each sensor's measurement axis intersecting at a single point. Minimizing the distance between this point and the sensors is essential in high-gradient regions, as small variations in the positioning can lead to inaccuracies in the measurement of the vector components. The assembly was devised to be compatible with a medium-to-large scale production, in order to minimize human handling, thus reducing assembly costs and improving repeatability. In previous designs, larger Hall sensor packages with lead wires were glued onto three faces of a glass cube, which was then attached to the PCB. This method required careful handling, leading to potential alignment errors. Connecting the leads involved threading a thin copper wire through the PCB and wrapping it around each sensor's leads, which was time consuming, challenging, and prone to inaccuracy [16].

The HG-0813 sensor features a compact SMD package with dimensions of $0.8\,\mathrm{mm} \cdot 1.6\,\mathrm{mm}$. The main challenge is the precise vertical placement of these SMD components. The final method involves constructing a 3-dimensional structure using custom one-dimensional PCBs. Two support PCBs, shown in figure 2 left, fixate and electrically connect the two vertical sensors. The sensor footprint is positioned precisely, and reflow soldering ensures accurate, reliable soldering of the SMD components. One unique PCB serves both the x- and y-axes by flipping the board and using the mirrored footprint. The interlocking of the two PCBs achieves high-precision placement. Once assembled, the support PCBs are inserted into the milled slots of the main PCB, where they are secured and electrically connected with solder joints. The final alignment, as seen in figure 2 right, shows that the sensors are accurately placed, with their measurement axes intersecting at a single point. This alignment process is quick and straightforward, an essential feature for supporting high production rates in the future.

The method is more robust than the previously used glass cube approach. In the glass cube method, the adhesive used to attach the Hall elements can degrade over time, and thermal or mechanical stresses from the cube and lead wires may compromise the long-term functionality of the probe. In contrast, the new design features Hall elements soldered directly onto a PCB, where they are both electrically connected and mechanically fixed by solder joints that are not susceptible to these effects.

The distance between the intersection point and each Hall element is approximately 1 mm, representing a 50% reduction compared to the glass cube method, which had a distance of 2 mm. The size of the Hall elements limits the distance, which could be further reduced with smaller packages. The precision of Hall element placement is constrained by the PCB manufacturer's fabrication tolerances, specified at ±0.1 mm, meeting the initial design requirements for high-precision measurements.

Although the angular alignment appears precise, some misalignment may still occur due to factors such as the Hall element's placement within the SMD package, potential chip displacement during soldering, and possible mechanical displacements in the interlocking PCBs. However, these limitations are mitigated by the calibration procedure described in section 5, which corrects any remaining misalignment. Using this procedure, section 6.2 verifies the alignment accuracy achieved with the newly developed alignment method.

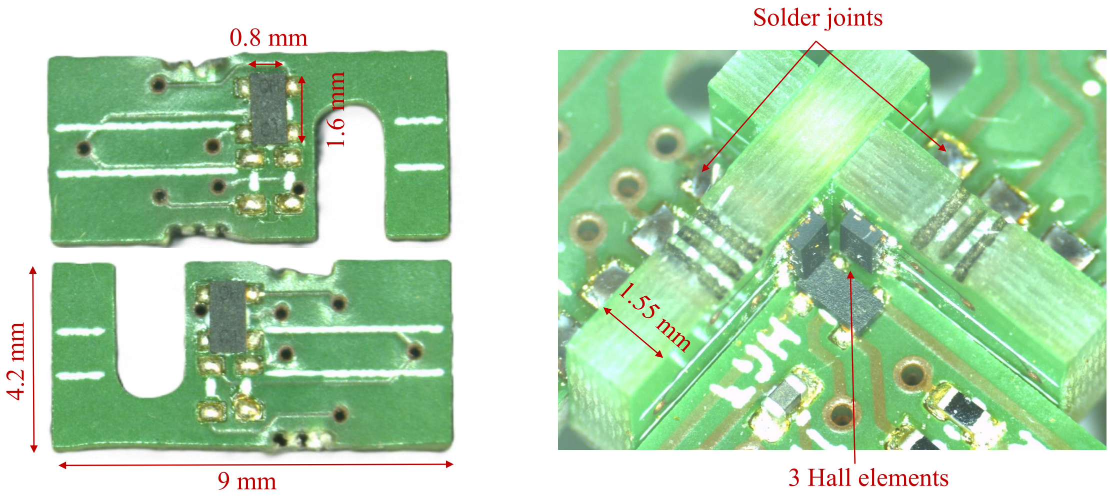

Figure 2. Support PCBs with soldered Hall elements (left) enabling precise 3D Hall element placement when inserted into the sensor card (right).

It is important to position the Hall elements as far as possible from magnetic materials, as these can distort the surrounding magnetic field and introduce measurement errors. Nearly every component contains some magnetic material; for example, the AD7124 includes 2.35% iron in its lead frames for cost reduction purposes [17]. Since non-magnetic materials are not feasible, a model of the AD7124 is simulated in Ansys Maxwell to assess its magnetic influence. Based on its material declaration, the ADC contains $m_{\mathrm{Fe}} = 6.79 \times 10^{-4}\,\mathrm{g}$ of iron [17]. Given iron's density $\varrho_{\mathrm{Fe}} = 7.874\,\mathrm{g\,cm^{-3}}$ [18] and the ADC's length $x = 5\,\mathrm{mm}$, the height of an equivalent iron cube representing the ADC's magnetic material is calculated as $h = \frac{m_{\mathrm{Fe}}}{\varrho_{\mathrm{Fe}} x^2} = 3.45\,\mu\mathrm{m}$. This equivalent iron cube model allows the simulation of the magnetic field variation around the ADC. In the simulation, the cube is placed in a uniform magnetic field ranging from 0.5 T to 4 T, covering the typical field strengths encountered in physics experiments. The influenced magnetic field is evaluated at various horizontal distances from the ADC. As can be seen in figure 3 left, the simulations indicate significant magnetic field changes in the order of 10^{-3} T within a 3 mm radius around the ADC. As seen in figure 3 right, the influence of the ADC increases with magnetic field strength and begins to saturate at around 3 T. Note the different unit of T^{-1}, which results in higher values for lower distortion. At lower fields, the nonlinear behavior of iron's permeability does not lead to significant additional distortion. Beyond the distance of 3 mm, the impact is minimal, suggesting that semiconductor components should be placed at least 3 mm from the Hall sensors to minimize magnetic influence.

However, this model does not include other components present on the card. Semiconductor devices such as the microcontroller, LDOs, and MOSFETs are also likely to contain iron in their lead frames [19]. In addition, standard resistors and capacitors often use nickel as an electrode material and for plating [20]. A full electromagnetic model including all components has not been developed, but the presence of additional magnetic materials suggests a greater potential for distortion. Therefore, placing the Hall elements as far as possible from other components is advisable.

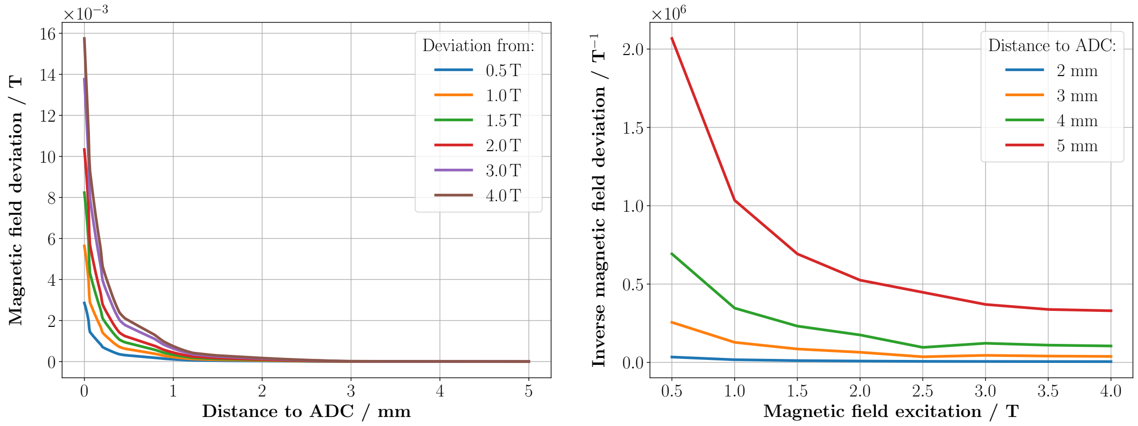

Figure 3. Simulation of magnetic field deviation at varying horizontal distances from the ADC model placed in a uniform field between 0.5 T and 4 T, using Ansys Maxwell.

4 Firmware architecture

The card is designed to serve as a data producing node within any CAN network. It supports the CANopen protocol, ensuring compatibility with other nodes in a CANopen communication network.

To identify each card within a network containing multiple cards, each card must have a unique serial number. This number is assigned during the card's programming process. The serial number can be modified using a SDO (Service Data Object) download, which updates the corresponding entry in the OD (Object Dictionary). The complete list of Object Dictionary entries is available in the CANopen documentation [5]. The serial number is also stored in flash memory to ensure its availability after power cycles. The default node ID of the sensor is 40. If multiple sensors with the same node ID are connected to the same network, it will cause the network to fail. To address this issue, the card supports LSS (Layer Setting Services) within the CANopen framework. When multiple nodes have the same node ID, the user can initiate a LSS command on the network. This command identifies each node by its unique serial number and assigns a unique node ID within the network, starting from 1 for the lowest serial number. The node ID is stored in flash memory, ensuring that the network configuration persists after a power cycle.

Upon powering on the card, it automatically performs offset and gain calibration for temperature and Hall voltage measurements, as detailed in section 2. By default, the measurement data is sampled and broadcast on the CANopen network at a period of 1 s. This period can be adjusted via a SDO download, which updates the corresponding OD entry. The data is transmitted through three Transmit Process Data Objects (TPDO1 to TPDO3), enabling fast real-time data transmission. Each of the three TPDO data frames contains 8 bytes of data, as detailed in table 1.

Table 1. Description of the data frames TPDO1 (message ID: 0x180 + node ID), TPDO2 (message ID: 0x280 + node ID), and TPDO3 (message ID: 0x380 + node ID).

Byte	Description
0	Measurement configuration of data (byte 1-3) - Bit 0-3: Do not care - Bit 4: 0 → unipolar measurement; 1 → bipolar measurement - Bit 5-6: ADC reference voltage; 00 → 0.6 V; 01 → 1.372 V; 10 → 2.5 V - Bit 7: ADC gain; 0 → gain = 1; 1 → gain = 2
1-3	Data for: - Hall sensor 1 (TPDO1) - Hall sensor 3 (TPDO2) - Temperature sensor (TPDO3)
4	Measurement configuration of data (byte 5-7). For details see byte 0
5-7	Data for: - Hall sensor 2 (TPDO1) - Hall sensor current (TPDO2) - Temperature sensor current (TPDO3)

The second operating mode supports synchronous transmission. When a SYNC message is sent on the network, each node samples its data and transmits it simultaneously through the three TPDOs. This mode is particularly useful when simultaneous measurements are required at variable time intervals. To complement the card's functionality, a desktop application developed in Python is available. This application enables users to utilize the described functionalities, receive measurement data, and visualize the results in real time.

5 Calibration of the Hall sensor card

Calibration is the key to an accurate magnetic field measurement. The electronic PCB measures the Hall voltages from three orthogonal Hall elements. Before calibration, there is no relationship between these voltages and the corresponding magnetic field values. This calibration method addresses this by mapping the measured voltages to magnetic field values while accounting for several non-ideal conditions and correcting for them.

5.1 Modeling of the calibration setup

The goal of the calibration model is to describe the voltage response of the Hall elements as a function of the magnetic field vector $\vec{B} = \left(B_x, B_y, B_z\right)$, using spherical harmonics [21]. Spherical harmonics form a set of orthogonal basis functions that enable continuous functions to be expressed as linear combinations of these basis functions. They are particularly useful for functions defined on the surface of a sphere, i.e., functions that map polar coordinates (r, θ, φ) to a scalar value. In this context, the magnetic field vector in Cartesian coordinates $(\vec{B})$ can be transformed into polar coordinates $(|\vec{B}|, \theta, \varphi)$, providing the basis for using spherical harmonics [22].

Equation 5.1 represents the Hall voltage model for a single Hall element. Here, N denotes the order of the spherical harmonic approximation, and K_l^m are the coefficients of the corresponding spherical harmonic functions Y_{lm}^{real}. Only real-valued spherical harmonics are relevant in this context. Further details, including the definition of spherical harmonics, can be found in [22].

$$V_{\text{Hall,Est}}\left(K_l^m\right) = \sum_{l=0}^{N} \sum_{m=-l}^{l} |\vec{B}|^l K_l^m Y_{lm}^{\text{real}}(\theta, \varphi) \tag{5.1}$$

The model does not include the temperature dependence of the Hall voltage. This omission is justified because the Hall voltage remains nearly constant over a broad temperature range, with a maximum temperature coefficient of only $-0.06\%/°\text{C}$ under constant excitation current conditions [13]. During calibration, the temperature is monitored, and the recorded fluctuations in the order of ±0.1 °C, have a negligible impact on the output voltage. Future work will focus on integrating temperature control systems into the calibration setup and incorporating temperature dependencies into the Hall voltage model to ensure accuracy across varying thermal conditions.

The calibration process involves measuring the Hall voltage for each of the three Hall elements under various magnetic field vectors $\vec{B}$. This is achieved by rotating the PCB within a uniform magnetic field of constant strength, which maintains a constant $|\vec{B}|$ while varying θ and φ. This rotation produces different measured Hall voltages, $V_{\text{Hall,Meas}}$. Each Hall element experiences a different orientation of $\vec{B}$ due to their orthogonality and generates therefore a different voltage. Consequently, each Hall element has its own set of coefficients K_l^m. These coefficients represent physical constants of each Hall element and correction factors. Increasing the order N of the approximation includes more correction factors, such as Hall coefficients, planar Hall coefficients, and electronic nonlinearities. Beyond the coefficients K_l^m, additional parameters are included in the model to account for angular misalignments affecting the angles θ and φ. These parameters correct for a non-ideal initial horizontal position of the Hall card, errors in the measured rotation angles θ and φ, and misalignments in the mechanical positioning of the Hall sensor elements. Precise knowledge of the field direction is not required, as the calibration reference frame is defined by the rotating plane of the calibration bench, and misalignments are incorporated into the model parameters.

5.2 Calibration procedure

During calibration, the card is rotated in a uniform and constant magnetic field using a rotation bench equipped with two piezoelectric motors from Tekceleo: a WLG-75-R motor for the θ rotation and a WLG-30-R motor for the φ rotation. The scan consists of 600 steps, during which the θ angle completes five full rotations and the φ angle completes six, effectively covering the surface of a sphere. At each step, the θ motor advances by 3° and the φ motor by 3.6°. The resulting orientations are shown in figure 4 left. Different colors indicate groups of 100 orientations, corresponding to one full rotation around the φ axis.

2025 JINST 20 P09003

At each measurement step, the motors stop, and the voltages from the three Hall elements, along with the corresponding angular positions, are recorded. Figure 4 right shows the complete calibration setup. The calibration bench, located inside the magnetic field, includes the Hall sensor card and the two rotation motors. The control system, which contains magnetically sensitive components such as transformers on the motor control boards, is placed outside the magnet. It includes a power supply for the control system and Hall card, two motor control boards from Tekceleo, an Arduino board for encoder readout, and a laptop running a Python script that coordinates the entire process. The script communicates with the motor control boards via USB to set the motor angles, reads the encoder positions from the Arduino, and acquires the Hall voltages from the Hall card over CAN.

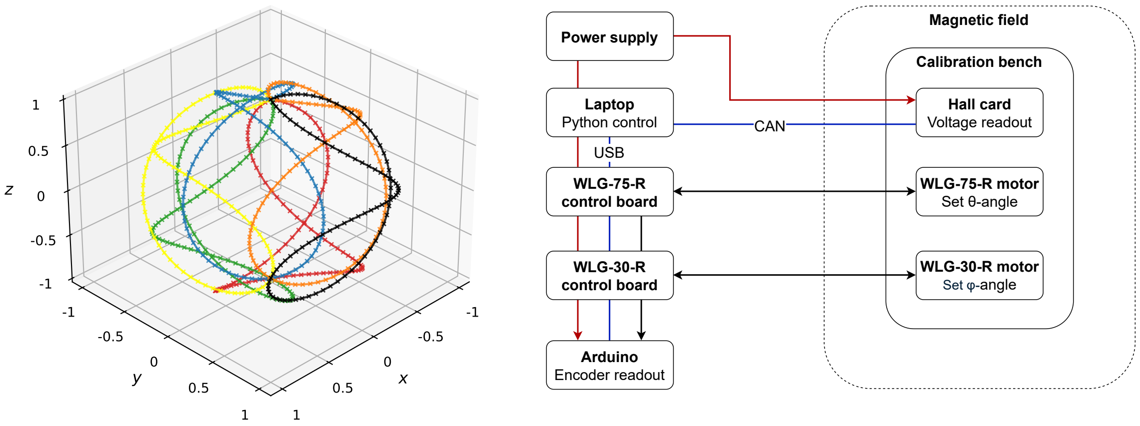

Figure 4. Covered orientations over the 600 calibration steps, corresponding to five full θ and six full φ rotations (left), and the calibration setup comprising the calibration bench with the Hall card and rotation motors inside the magnetic field, and the control system located outside due to magnetic sensitivity (right).

After recording the Hall voltages and magnetic field vectors $\vec{B}$ over the 600 steps, the residual function defined in equation (5.2) is minimized using a least-squares optimization with the Trust Region Reflective algorithm. This process yields the complete set of model parameters describing the system.

$$f\left(K_l^m\right) = V_{\text{Hall,Est}}\left(K_l^m\right) - V_{\text{Hall,Meas}} \tag{5.2}$$

After calibration, knowing the coefficients K_l^m and the measured voltages allows the numerical solution of equation (5.1), yielding the magnetic field vector either in spherical coordinates $(|\vec{B}|, \theta, \varphi)$ or in Cartesian form (B_x, B_y, B_z).

6 Experimental results

6.1 Electronic readout behaviour

This section describes the measurements conducted to evaluate the reliability of the electronic readout in strong magnetic fields. To achieve this, a constant 50 mV DC voltage, generated by a Keithley 2410 source meter, was applied to the output pads of the three Hall elements, which were removed during the test. To assess measurement precision and the influence of the magnetic field, four different measurements were performed.

In the first configuration, the sensor card was placed horizontally inside a laboratory magnet. In the second configuration, the card was rotated inside the magnet, following the calibration routine described in section 5. In both configurations, 600 samples of the voltages on each sensor readout (V_x, V_y, V_z) were recorded over approximately 60 min, both in the presence of a 0.225 T magnetic field and without a magnetic field.

The test field of 0.225 T was chosen because it corresponds to a coil current of 150 A in the calibration magnet, which simplifies repeatability and setup. This operating point provides a practical and reproducible reference field that enables stable testing of the sensor response, without approaching saturation limits of the magnet or the readout electronics. The magnetic field is provided by CERN's MNP-17 dipole magnet, which features a field uniformity of ±40 µT within the calibration volume of $10\,\mathrm{cm} \cdot 10\,\mathrm{cm} \cdot 10\,\mathrm{cm}$, a field stability of $\pm 30\,\mu\mathrm{T\,h^{-1}}$, and a temperature stability of up to ±0.1 °C. This temperature variation has a negligible effect on the Hall element output, given its temperature coefficient of $-0.06\%/°\mathrm{C}$, which corresponds to a voltage shift of approximately 3 µV at a field strength of 0.225 T.

Figure 5 left shows the mean errors and standard deviations between the four measurements and 50 mV. The measurements are consistent across all three axes in each configuration. The mean values and standard deviations remain within 1 µV, indicating stable measurements. When the sensor card is stationary, the presence of a magnetic field has no effect on the measurement. However, when the sensor card rotates, the magnetic field increases the standard deviation to approximately 2 µV. This slightly higher noise can be explained by small voltages induced in the cables connecting the source meter to the card, which arise during rotation within the magnetic field. Although the contribution of the electronic components themselves cannot be entirely excluded, further evidence for cable-induced artifacts was observed. Manually adjusting the cables during rotation (e.g., to unwind twisting) resulted in noticeably larger voltage fluctuations compared to when the cables remained untouched. In normal operation, these cables are not present and therefore will not influence the measurement.

In the future, the readout is intended to be used in stronger magnetic fields. Although rotation cannot currently be performed in fields above 1 T, it is possible to test the readout in a stationary configuration at fields above 2 T using a magnet with a smaller gap size. For this, the magnetic field is generated by CERN's PT-7 dipole magnet, which provides a field of 2.3 T at a current of 600 A, the maximum current at which the coil temperature remains stable without overheating. For tests conducted at 2.3 T, the RMS noise level remains in the order of 2 µV, comparable to the tests performed at lower field strengths, supporting the observation that noise remains negligible even at higher fields. Reliable measurements that are unaffected by external magnetic fields are crucial. The small standard deviations and RMS noise levels, within 2 µV, proof good stability and precision.

6.2 Hall element alignment precision

Precision in the simple assembly process of the Hall elements, as described in section 3, is essential for the sensor card's development. To correct for misalignments introduced during assembly, two angles, θ_{corr} and φ_{corr}, are defined as correction parameters for each Hall element in the Hall voltage model. A third parameter, the rotation of the Hall element around its normal axis, would be required to fully describe its misalignment. However, this degree of freedom is captured by the linear combination of components in the spherical harmonic expansion. Adding this extra angle to the model does not change the optimization result, as it yields the same cost function value and is

2025 JINST 20 P09003

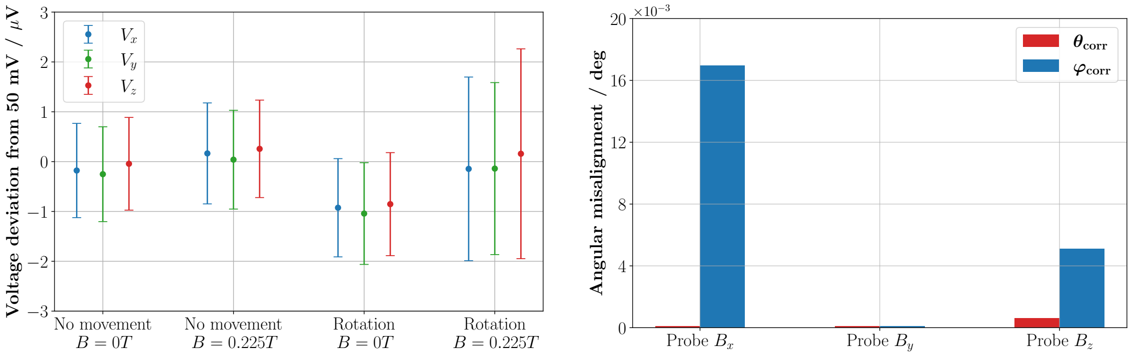

Figure 5. Mean value and standard deviation of the error between the measured voltage and the applied 50 mV with a stationary and a rotating Hall card, both with and without an external magnetic field (left) and angular misalignment of the Hall elements (right).

therefore redundant. As a result, the system model incorporates six correction angles, representing the orientation offset of the Hall elements.

To obtain a complete description of the system and its parameters, the calibration procedure described in section 5 is carried out using the experimental setup introduced in section 6.1. The calibration is based on a spherical harmonic expansion up to order $N = 3$ to account for nonlinearities in the system. A constant magnetic field of 0.45 T is selected for this measurement, as it lies near the midpoint of the intended measurement range (centered around 0.5 T) and provides an equidistant step from the earlier measurement at 0.225 T.

Figure 5 right shows the correction angles of the three Hall elements. The largest parameter, the φ_{corr} angle of the B_x probe, converges to approximately 0.016°, with most other values being even smaller. Although this demonstrates the effectiveness of the proposed method, reproducibility is not guaranteed, as the measurement was performed on a single manufactured PCB. However, in full-scale production, industrial solder paste printers and pick-and-place machines will improve the precision of component placement.

6.3 Magnetic field measurements

These results describe the performance of the calibration and the resulting field measurement accuracy. The evaluation of the calibration fit is based on the calibration presented in section 6.2, which quantifies the alignment precision. Figure 6 shows both the measured voltages and those calculated from the fitted model. It also displays the residuals between them, which remain consistently within the order of 10^{-4} V. The residuals are small but show a systematic pattern that is not attributable to known physical phenomena. One possible source of this behavior is the presence of nickel in the ENIG (Electroless Nickel Immersion Gold) surface finish of the PCBs. When a solder pad with an ENIG finish is positioned above the Hall elements, voltage variations in the order of 10^{-4} V can be observed. To mitigate this effect, future PCB revisions will skip the surface finish entirely, exposing bare copper pads.

To assess the accuracy of the magnetic field calculation, each of the 600 sets of measured voltages is used to solve the fitted model for the field components $|\vec{B}|$, θ, and φ. Table 2 reports the mean value of the residuals between the measured field vectors and the reconstructed ones. The magnitude of the field is measured using Metrolab's NMR (Nuclear Magnetic Resonance) teslameter with an

2025 JINST 20 P09003

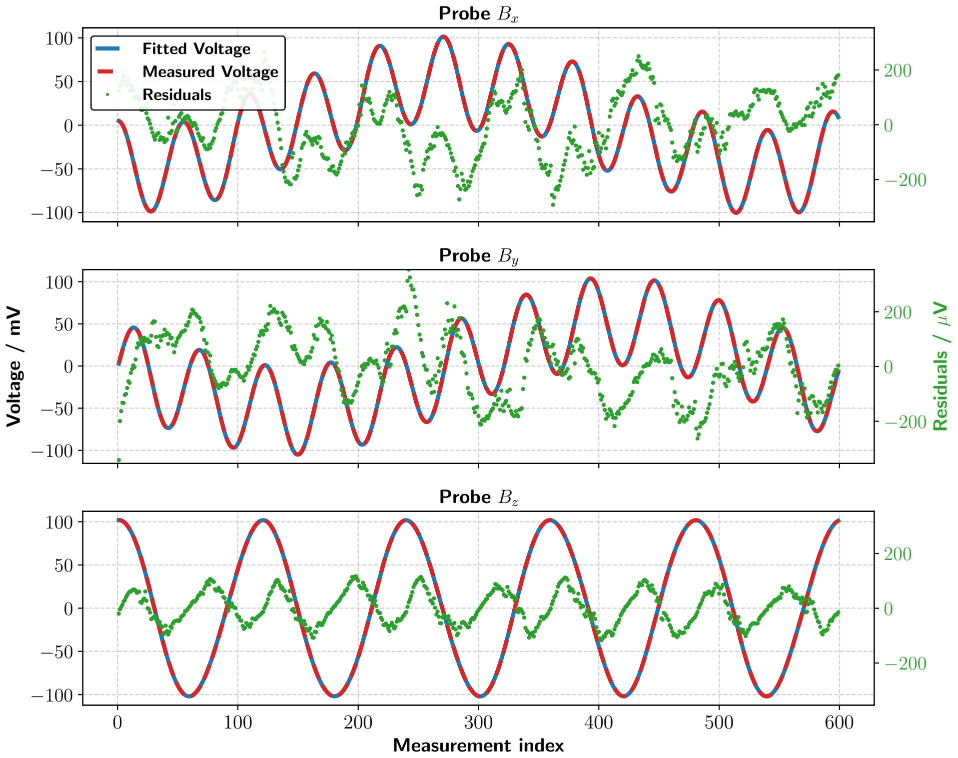

Figure 6. Measured and fitted voltages of the three Hall elements, along with their corresponding residuals. Note the different axis scaling used for the residuals. The calibration is performed on 600 measurement points over 5 rotations of θ and 6 rotations of φ in a uniform field of 0.45 T.

Table 2. Mean residuals between the measured and reconstructed field vectors of a calibrated Hall card at three different field strengths.

Field strength	**Mean($\lvert\Delta\lvert\vec{B}\rvert\rvert$)**	**Mean($\lvert\Delta\theta\rvert$)**	**Mean($\lvert\Delta\varphi\rvert$)**
0.225 T	4.6×10^{-5} T	0.083°	0.666°
0.45 T	6.2×10^{-5} T	0.059°	0.547°
0.675 T	8.8×10^{-5} T	0.064°	0.548°

accuracy of ±5 ppm [23], while the angles are obtained from the built-in motor encoders with a resolution of 0.045° (WLG-30-R) and 0.0156° (WLG-75-R) [24]. This evaluation is repeated under the same experimental conditions as in section 6.2 for two additional field strengths, 0.225 T and 0.675 T, resulting in three equidistant measurement points. This allows assessment of the model's performance across varying magnetic field conditions.

A trend of increasing mean error in reconstructing the magnetic field strength is observed with increasing field strength, from 4.6×10^{-5} T at 0.225 T to 8.8×10^{-5} T at 0.675 T. This increase follows the rising absolute field values. Nevertheless, the maximum mean error remains below 0.02% of the total field, demonstrating a high accuracy of the calibration model.

The mean errors in angular reconstruction remain stable across the tested range. The polar angle error decreases from 0.083° at 0.225 T to 0.059° at 0.45 T, then slightly increases to 0.064°

2025 JINST 20 P09003

at 0.675 T. The azimuthal angle error drops from 0.666° to around 0.547°, with minimal variation between 0.45 T and 0.675 T. This stability indicates that the angular reconstruction performance is largely independent of the field strength and remains robust across the tested range.

7 Conclusion

This research presents a method for measuring strong magnetic fields up to 1 T using a custom PCB and a 3-dimensional Hall sensor array, characterized through spherical harmonics. The innovative Cartesian assembly of the Hall elements achieves high precision with a straightforward alignment process, resulting in a more robust design and reducing the intersection-to-element distance to 1 mm, compared to 2 mm in previous designs. Combined with the reliability of the voltage readout, this enables accurate field measurements that meet the initial requirements.

The novel spherical harmonic calibration model achieves reconstruction accuracies with a maximum mean error of 8.8×10^{-5} T for the field magnitude, 0.083° for the polar angle θ, and 0.666° for the azimuthal angle φ. These results were validated through rotational calibration in uniform fields of 0.225 T, 0.45 T, and 0.675 T. The field magnitude error of 8.8×10^{-5} T exceeds the initial accuracy requirement of 10^{-4} T. The reconstruction of θ is close to the target accuracy of 0.06°, while φ reconstruction falls short by approximately a factor of 10. Overall, the system achieves a field magnitude reconstruction precision in the order of 0.02%, representing a notable improvement over previous designs, which were limited to approximately 0.07% [3].

These results demonstrate that the approach is well suited for scalable, sensor-based, high-precision magnetic field mapping systems, potentially using up to 200 sensor cards, particularly in the context of high-energy physics experiments. Future work will focus on improving the calibration system to enhance accuracy, particularly for φ reconstruction. Planned improvements include redesigning the PCB without a surface finish to mitigate nickel-related effects, enhancing the calibration software, and introducing temperature control to account for temperature-dependent Hall voltage variations. In addition, future developments will target real-time inverse solutions under non-uniform field conditions up to 4 T, in line with experimental requirements. An evaluation of the cards' radiation hardness is also planned.

Acknowledgments

This work was partly supported by the *Österreichische Bundesministerium für Wissenschaft, Forschung und Wirtschaft* (Austrian Federal Ministry of Science, Research and Economy). We would also like to thank Matthias Mentink (CERN) for his valuable assistance in validating some of the simulations.

References

[1] T.M. Taylor, *The magnets for the LHC experiments*, *IEEE Trans. Appl. Supercond.* **10** (2000) 342.

[2] M. Aleksa et al., *Results of the ATLAS solenoid magnetic field map*, *J. Phys. Conf. Ser.* **110** (2008) 092018.

[3] V.I. Klyukhin et al., *Measurement of the CMS Magnetic Field*, *IEEE Trans. Appl. Supercond.* **18** (2008) 395 [`arXiv:1110.0306`].

[4] J.R. Fry, G. Ruggiero and F. Bergsma, *Precision magnetic field mapping for CERN experiment NA62*, *J. Phys. G* **43** (2016) 125004.

[5] CAN in Automation e.V., *CiA 301 version 4.2.0. CANopen application layer and communication profile*, 2011.

[6] M. Losasso et al., *Tests and Field Map of LHCb Dipole Magnet*, IEEE Trans. Appl. Supercond. **16** (2006) 1700.

[7] LHCb collaboration, *LHCb magnet: Technical design report*, CERN-LHCC-2000-007 (2000).

[8] Microchip Technology Inc., *MIC5219, 500 mA Peak Output LDO Regulator*, 2018.

[9] Quantek Technology Corporation, *QC5CB Series 3.2x5.0 2-Pad SMD All Ceramic Crystal Unit*, 2024.

[10] Analog Devices, *AD7124-8, 8-Channel, Low Noise, Low Power, 24-Bit, Sigma-Delta ADC with PGA and Reference*, 2023.

[11] TDK Electronics Corporation, *Temperature protection device. Chip NTC thermistor*, 2023.

[12] A. Kalnoskas, *Error analysis in temperature sensing with NTC and silicon-based PTC thermistors: Comparing the Ratiometric and Absolute methods*, 2019.

[13] Asahi Kasei Microdevices, *GaAs Hall Element HG-0813*, 2021.

[14] Texas Instruments, *REF4132 Low-Drift, Low-Power, Small-Footprint Series Voltage Reference*, 2020.

[15] M. Zamora, *Precision Current Sources and Sinks Using Voltage References*, Texas Instruments (2020).

[16] H. Boterenbrood, *B-sensor with addressable Serial Peripheral Interface*. CERN, NIKHEF (2001).

[17] Analog Devices, *Materials Declaration for AD7124-8*, 2024.

[18] Thomas Jefferson National Accelerator Facility — Office of Science Education, *The Element Iron*, 2024.

[19] STMicroelectronics, *Materials Declaration Form for STM32L443CCT6*, 2023.

[20] Bourns, *Material Declaration Sheet for CRT Series*, 2024.

[21] F. Bergsma, *Calibration of hall sensors in three dimensions*, presented at the *13th International Magnetic Measurement Workshop*, Stanford, California, U.S.A., May 19–22 (2003).

[22] V. Schönefeld, *Spherical harmonics*, Technical Note, Computer Graphics and Multimedia Group, RWTH Aachen University, Germany (2005).

[23] Metrolab Instruments SA, *PT2025 NMR Teslameter User's manual*, 2003.

[24] Tekceleo, *Wavelling Catalog. High Performance Piezoelectric Actuators*, 2023/2024.